Journal of Oceanology and Limnology

https://doi.org/10.1007/s00343-026-5295-1

Research Paper

Research on the response of the upper ocean to typhoons*

Yu QI[1, 2, 3], Ying WANG[1, 2, **]

[1] *State Key Laboratory of Climate System Prediction and Risk Management, Nanjing University of Information Science and Technology, Nanjing 210044, China*

[2] *School of Marine Sciences, Nanjing University of Information Science and Technology, Nanjing 210044, China*

[3] *College of Ocean and Earth Sciences, Xiamen University, Xiamen 361102, China*

Received Aug. 14, 2025; accepted in principle Oct. 14, 2025; accepted for publication Dec. 15, 2025

Abstract Typhoon, as one of the most destructive weather systems, causes significant impacts on the marine environment. We established a multi-dataset case-comparative framework by integrating Argo buoy observations, HYbrid Coordinate Ocean Model (HYCOM) reanalysis data, and Integrated Multi-satellitE Retrievals for GPM (IMERG) satellite precipitation data, to elucidate the upper ocean response mechanisms to four distinctive typhoons in the northwest Pacific (2021–2024). Our analysis revealed several key mechanistic insights. Results show that the HYCOM model can simulate the temperature and salinity trends, but systematically underestimates precipitation dilution (with salinity deviations of 0.1–0.2) and mixing intensity (with temperature deviations of 0.4–1.2 °C), due to insufficient parameterization of the wind-wave-current coupling process. After typhoon passage, sea surface temperature decreases sharply by 1.5–3 °C due mainly to the enhanced vertical mixing, while salinity decreases by 0.1–0.6 as a result of the combined effects of precipitation dilution and mixing with deep high-salinity water. The mixed layer depth (MLD) increases from 40 to 100 m. The temperature recovers gradually within 10 d due to solar shortwave radiation and advection, while salinity recovers more slowly due to its conservative nature. A notable asymmetry was observed, and the Ekman suction driven by strong winds was enhanced on the right side of the typhoon track, leading to a significantly deeper disturbance depth compared to the left side. Significant thermal anomalies were observed in the subsurface (80–500 m), resulting from the competing effects of vertical mixing and Ekman pumping. The cold wake is primarily governed by wind-driven vertical mixing, while its spatial pattern is co-regulated by precipitation-induced freshwater input. Ekman transport plays a critical role in subsurface heat redistribution. These findings underscore the importance of multi-platform observations for understanding complex ocean responses and highlight key areas for improving coupled model parameterizations.

Keyword: typhoon; upper ocean; response; Array for Real-time Geostrophic Oceanography (Argo); HYbrid Coordinate Ocean Model (HYCOM)

1 INTRODUCTION

A typhoon is an intense cyclonic vortex that develops over tropical or subtropical oceanic surfaces, characterized by sustained wind speed exceeding 32.7 m/s. The northwest Pacific is the most active basin for tropical cyclones globally, contributing to over 30% of worldwide typhoon occurrences (Wang et al., 2024c). When a typhoon moves into colder waters or encounters strong vertical wind shear, its energy supply from the warm water layer is disrupted, leading to a weakening of the typhoon, eventually dissipating (Emanuel, 1995; Tan et al., 2024; Wu et al., 2024). The life cycle of a typhoon is governed by large-scale atmospheric circulation systems (e.g., the subtropical high and monsoon troughs), while also being strongly influenced by oceanic thermal conditions such as sea surface

* Supported by the National Key R&D Program of China (No. 2024YFC2815703) and the National Natural Science Foundation of China (No. 41905089)

** Corresponding author: wangying_thw@nuist.edu.cn

temperature (SST) and the thickness of warm water layer. Recent research has demonstrated that the spatial variation of SST plays a critical role in modulating typhoon intensity. The Warm-Core Pattern strengthens secondary circulation within the typhoon's inner core region and enhances latent heat flux absorption, thereby facilitating system intensification. Conversely, the Poleward-Decreasing Pattern inhibits ocean-to-atmosphere energy transfer, resulting in typhoon weakening (Sun et al., 2024). This finding challenges the conventional assumption of uniform SST in numerical models, offering novel insights for typhoon intensity prediction. Against the backdrop of global warming, SST has increased by 0.1–0.2 °C per decade, contributing to more intense typhoons and a northward migration of their tracks (Intergovernmental Panel on Climate Change, 2021). Variations in atmospheric humidity and vertical wind shear also affect the genesis location and trajectory typhoons (Kossin et al., 2020). A notable example is the El Niño-Southern Oscillation (ENSO), which alters typhoon formation frequency through its modulation of the spatial extent of the tropical western Pacific warm pool (Tan et al., 2024). However, oceanic factors such as salinity stratification and mesoscale eddies may partially counteract warming-induced effects, leading to substantial regional variability in typhoon behavior (Zhou et al., 2019; Guan et al., 2024; Liu et al., 2024).

Typhoons exert profound influences on the marine environment, through powerful wind forcing, intense precipitation and massive waves. These forcing induce not only substantial SST variation but also trigger a cascade of oceanic responses, including mixed layer deepening, subsurface thermal restructuring, and ocean currents reorganization (Brizeula et al., 2023). The passage of a typhoon induces a pronounced SST reduction through vertical mixing and upwelling, generating a distinct cold wake (Zhang et al., 2019a; Yu et al., 2023). This process simultaneously deepens the ocean mixed layer by 50–100 m through wind stress, entraining colder subsurface waters that modify the oceanic thermal and saline structure. Prolonged heavy rainfall resulted in a significant salinity decrease in the upper ocean and the convergence of upper water deepened the thermocline and the mixed layer (Wang et al., 2023a). The upper ocean characteristics, particularly temperature, salinity, and current patterns, play fundamental roles in typhoon genesis, evolution, and decay. Warmer SST supplies essential heat and moisture for typhoon development, while mesoscale processes such as oceanic eddies critically modulate the typhoon intensity and track (Wang et al., 2024a). Specifically, warm eddies delay mixed layer deepening through their large heat content, minimizing SST cooling and sustaining typhoon intensity, whereas cold eddies promote rapid energy dissipation leading to its weakening (Jyothi and Joseph, 2019). Besides, the presence of the cold-core eddy contributes to the stronger along-track cold advection, which dominates the increase in the sea surface cooling near the radius of maximum wind to the right of the typhoon track. Meanwhile, the stronger cross-track warm advection acts to prevent the cooling induced by the vertical mixing (Li et al., 2022).

Upper ocean dynamics under typhoon forcing have emerged as a key research focus in air-sea interactions. Combining multi-source satellite data (microwave radiometers, infrared sensors) with Array for Real-time Geostrophic Oceanography (Argo) buoy profiles, researchers now track high-resolution SST anomalies, wind stress, and 3D thermal-saline structures during typhoon events. These integrated approaches overcome traditional observational limits, enabling systematic analysis of mixed-layer dynamics and air-sea energy exchange (Yang et al., 2010; Zhang et al., 2019b; Ni et al., 2021). Particularly, the comparative analysis of cases using dedicated observation arrays have significantly advanced our understanding of the complex ocean response. For instance, an array of buoys and moorings captured the detailed three-dimensional thermohaline and dynamical responses to Typhoon Kalmaegi (2014), revealing a three-layer vertical structure in temperature and salinity anomalies and the dominant role of the first baroclinic mode in near-inertial currents, which were corroborated by numerical model simulations (Zhang et al., 2016). Liu et al. (2022) revealed pronounced spatiotemporal heterogeneity in typhoon-induced cooling from Typhoon Lekima in the Yellow Sea, with coastal regions exhibiting stronger temperature drops than offshore areas, attributable to enhanced tidal mixing near shore. Kawakami et al. (2022) pointed out that in the Kuroshio Extension region, the cooling effect of typhoons is limited due to a deep mixed layer greater than 200 m and weak temperature gradients, with SST cooling magnitude of only 0.8–1.2 °C.

Additionally, the near-inertial currents and Ekman currents, driven by typhoon wind stress with

a period of approximately 12 h, are essential to the upper ocean dynamic response. Based on buoy observations, Fan et al. (2022) found a pronounced hemispheric asymmetry in typhoon-induced near-inertial currents, with 30%–50% stronger kinetic energy and more significant salinity anomalies on the right side of the typhoon track in the Northern Hemisphere. Recent advancements in autonomous ocean observation technologies are further revolutionizing data collection within the high-impact core of typhoons. As an illustration, during super Typhoon Koinu (2023), an array of unmanned vehicles (underwater gliders and wave gliders) successfully probed the inner-core air-sea conditions, providing unprecedented measurements of atmospheric parameters, SST, and subsurface thermohaline structure near the typhoon center (Zhang et al., 2024). Such direct observations from mobile platforms are invaluable for validating and improving the performance of ocean models and coupled forecast systems under extreme wind conditions. On the right side of the typhoon, a deeper and more persistent barrier layer forms due to heavy rainfall, with an average thickness approximately twice that on the left side. The barrier layer suppresses the entrainment mixing in the upper ocean, thereby reducing the cooling caused by the entrainment of cold water from the lower layer (Zhang et al., 2025). This asymmetry is closely related to the wind field and precipitation distribution. Typhoons dynamically can alter mixed layer structure through wind-driven Ekman suction and turbulent mechanical stirring (Woodruff et al., 2013; Zhang et al., 2021, 2023; Wang et al., 2022). Typhoon-induced sea level anomalies result from combined wind-driven water piling, cold tail currents, and tidal effects. Current limitations include inadequate observations of subsurface flows and internal ocean dynamics during typhoons, plus insufficient coupled modeling. Future research should integrate multi-source, high-resolution data to improve typhoon-ocean interaction forecasts for disaster prevention and climate assessment.

The typhoon triggered substantial sea surface cooling, mainly driven by intensified vertical mixing and Ekman pumping, with the cold wake being modulated by pre-existing mesoscale eddies (Li et al., 2022). Typhoon-induced mixing modulates the warm surface water into the subsurface, and typhoon-induced advection further modulates the warm water into the deeper ocean and influences the ocean heat budget (Zhang, 2023). Additionally, the oceanic cooling feedback inhibited the maintenance of the typhoon's intensity by reducing air-sea heat fluxes, while the strong wind stress and precipitation induced by the typhoon further altered the thermohaline structure and circulation in the upper ocean, highlighting the critical regulatory role of air-sea coupling processes in typhoon-ocean interactions (Li et al., 2023). To better understand the response characteristics and mechanisms of the upper ocean to typhoon forcing in the northwest Pacific, this study employs multiple data sources, including Hybrid Coordinate Ocean Model (HYCOM) reanalysis data and Argo observations, to systematically analyze spatiotemporal variations in upper ocean physical parameters under tropical cyclone impacts, elucidating the underlying dynamical and thermodynamical processes governing these responses. The structure of this manuscript is as follows. Section 2 introduces the datasets and research methods used in this study. Sections 3 and 4 analyze the temporal and spatial response characteristics of the upper ocean to typhoons using Argo observational data and HYCOM reanalysis data, respectively. Section 5 presents the conclusions and discussions of this study.

2 DATA AND METHODOLOGY

The best track dataset for typhoons is provided by the China Meteorological Administration Tropical Cyclone Data Center (Ying et al., 2014; Lu et al., 2021). Figure 1a shows the tracks of the 77 typhoons that occurred in the northwest Pacific basin from January 1, 2021 to December 31, 2024. The temporal resolution of this dataset is 3 h.

The Argo data were obtained from the China Argo Real-time Data Center, which provides real-time observations from Chinese buoy. The dataset also includes comprehensive buoy observations transmitted via advanced satellite such as Argos, Iridium, and BeiDou. Figure 1b illustrates the successfully matched buoy, with their information detailed in Table 1.

The HYCOM reanalysis data (Wallcraft et al., 2009), basing on an advanced ocean model and data assimilation system, provides global ocean key variables such as ocean circulation, temperature, and salinity with a high spatial resolution of 1/12°×1/12°. In this study, we utilized the HYCOM dataset generated by the Global Ocean Forecast System (GOFS) 3.1 on the GLBy0.08 grid. Additionally, hourly surface wind field data with a spatial

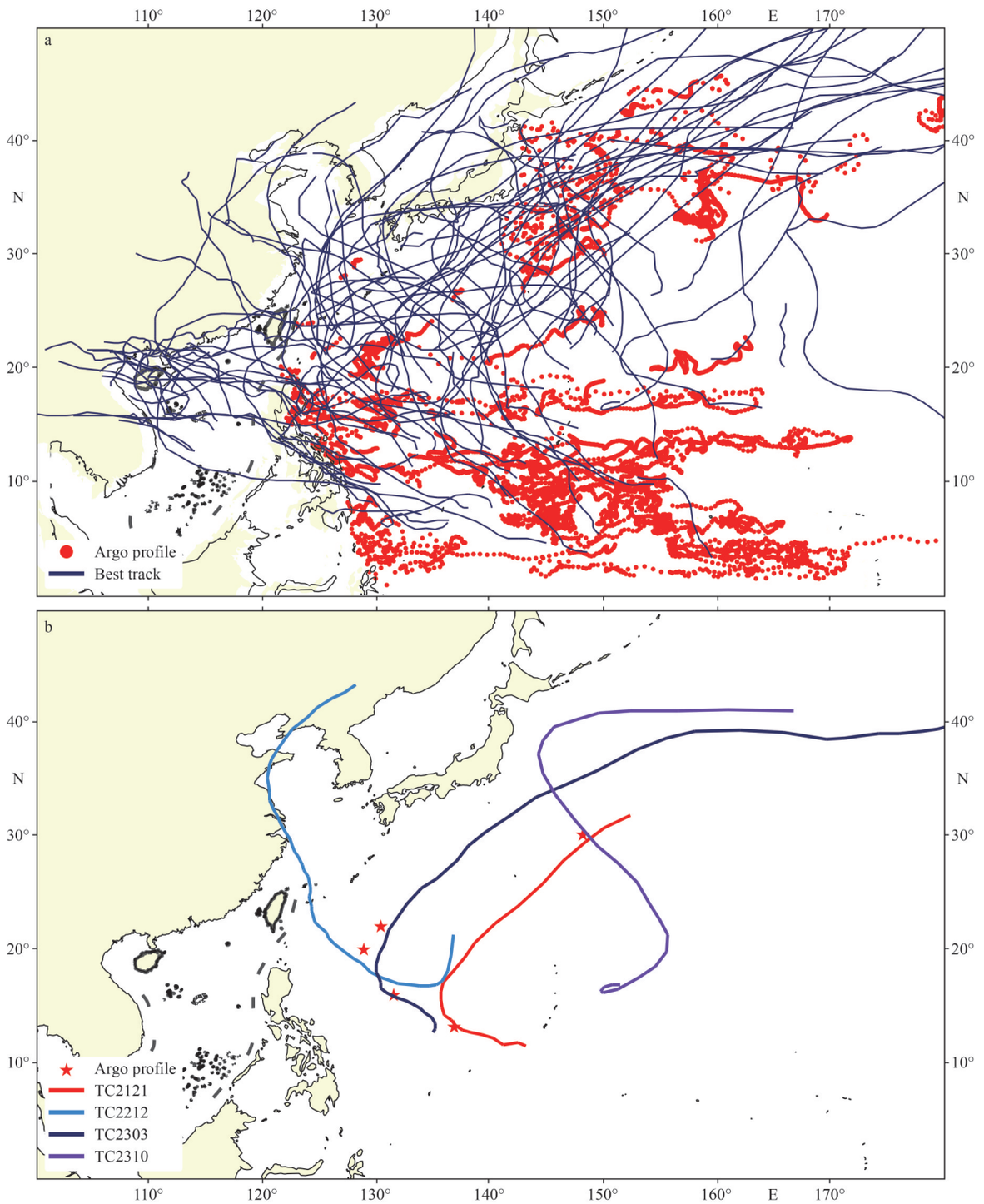

Fig.1 Typhoon tracks and Argo profile locations

a. in the relevant ocean basin from January 1, 2021 to December 31, 2024. Red dots indicate Argo profile positions, and blue solid lines represent typhoon tracks; b. in four representative cases. The red stars indicate the locations of successfully matched Argo profiles. The red line represents Typhoon Nyatoh (TC2121), the light blue line represents Typhoon Muifa (TC2212), the dark blue line represents Typhoon Guchol (TC2303), and the purple line represents Typhoon Damrey (TC2310).

resolution of 0.25°×0.25° were obtained from the Climate Forecast System Reanalysis (CFSR) provided by the National Centers for Environmental Prediction (NCEP).

The Global Precipitation Measurement (GPM) precipitation data is jointly developed by the National Aeronautics and Space Administration (NASA) and the Japan Aerospace Exploration Agency (JAXA). It

Table 1 Details of the successfully matched Argo buoy

Number	WMO ID	Type	Update frequency	Longitude	Latitude
519	2902847	HM2000	1 d	138.85°E	10.90°N
555	2902880	XUANWU	2 d	130.51°E	20.16°N
556	2902881	HM2000-O2	5 d	134.84°E	24.21°N
564	2902887	PROVORIV_FLBB	1 d	150.00°E	30.00°N

integrates observations from multiple satellites along with ground-based precipitation measurements, offering high temporal and spatial resolution capable of accurately capturing the complex precipitation patterns induced by typhoons. In this study, we derived the precipitation observations from the Integrated Multi-satellite Retrievals for GPM (IMERG) product, which combines data from the GPM Microwave Imager (GMI) and the Dual-frequency Precipitation Radar (DPR). The IMERG dataset provides precipitation information at a spatial resolution of 0.1°×0.1° and a temporal resolution of 30 min (Huffman et al., 2019).

A primary challenge in analyzing typhoon-ocean interactions involves establishing precise spatiotemporal correspondence between typhoon track and observational data, which is fundamental for accurately quantifying upper ocean responses. In this study, 77 typhoon cases that occurred over the northwest Pacific from 2021 to 2024 were selected, along with more than 8 300 Argo profiles, as shown in Fig.1a. Using a spatiotemporal matching criterion (200-km radius, ±1-d window) relative to tropical cyclone tracks from the China Meteorological Administration's Best Track Dataset. This criterion follows established methodologies in similar studies (Sun et al., 2023) to capture the core oceanic response while accounting for typical typhoon translation speeds and observational coverage. Through this process, we identified 38 qualifying Argo profiles. To ensure representativeness, the four typhoon cases (Typhoon Nyatoh, Typhoon Muifa, Typhoon Guchol, Typhoon Damrey) were selected for detailed analysis based on two criteria: comprehensive Argo data coverage within the influence radius, and a range of typhoon intensities, as shown in Fig.1b.

In Fig.1b, the red line represents the track of Typhoon Nyatoh (No. 21 in 2021). This typhoon originated in the northwestern Pacific near 14°N/138°E and is classified as an offshore typhoon with a northwestward-recurving path. It reached a peak intensity of a severe tropical storm, with maximum winds of 28 m/s and a minimum pressure of 982 hPa. Influenced by the eastward retreat of the subtropical high, the typhoon remained mainly over the ocean east of the Philippines, without a direct landfall in China.

The light blue line in Fig.1b depicts the track of Typhoon Muifa (No. 12 in 2022), marking China's most intense landfalling typhoon of the year and the first since 1949 to strike four provinces. Following a northwestward track with inland recurvature, Muifa first made landfall on September 14 at Zhujiajian Island, Zhejiang Province (45 m/s, 950 hPa) as a strong typhoon, then weakened upon second landfall in Fengxian District Shanghai (33 m/s, 970 hPa) on September 15. Subsequent tropical storm-force landfalls in Shandong's Qingdao and Liaoning's Dalian established its unprecedented cross-regional passage from eastern to northeastern China, with a heavy rainfall that effectively alleviated drought conditions along Changjiang (Yangtze) River basin-highlighting its dual role as both a disaster-causing and water-supplying system.

The dark blue track in Fig.1b corresponds to Typhoon Guchol (No. 3, 2023) that originated east of the Philippines (12°N, 135°E). As a classic westward-propagating typhoon, its motion was predominantly controlled by the steering flow of subtropical high. Guchol intensified to a strong typhoon (48 m/s, 945 hPa), advancing northwestward at 20–25 km/h.

The purple track in Fig.1b indicates Typhoon Damrey (No. 10, 2023), which formed near Guam (13°N, 145°E) and underwent a rapid northeastward recurvature. Notable for its exceptional translation speed, Damrey peaked as a tropical storm (28 m/s, 988 hPa) before completing extratropical transition near Japan's Beppu Bay Influenced by the pre-trough flow of the mid-latitude westerlies, its track shifted significantly eastward and did not directly affect Chinese mainland.

To investigate the response of upper-ocean surface and subsurface temperature and salinity to typhoons, we used gridded HYCOM reanalysis data for analysis, and computed temperature and salinity

anomalies using a relative change algorithm based on reference baseline fields. Using HYCOM reanalysis data from the 7-d period preceding typhoon passage, average temperature and salinity values were calculated for each grid point to construct three-dimensional baseline fields. Subsequently, during the typhoon passage, anomalies were derived as the deviation between observed values at that time point and the corresponding baseline values. This calculation method has been widely applied in typhoon-ocean interaction studies (Yang et al., 2019b), effectively identifying ocean thermal anomaly signals associated with typhoon passage.

Since the HYCOM model data used in this study did not directly provide vertical velocity within the ocean, the vertical density-driven flow was calculated based on the continuity equation Eq.1 (Zhu and Ke, 2009), and regarded as the vertical velocity of seawater as expressed in Eq.2 below:

$$\frac{\partial u}{\partial x}+\frac{\partial v}{\partial y}+\frac{\partial w}{\partial z}=0, \tag{1}$$

$$\omega(z_k)=\omega(z_{k-1})-\int_{z_{k-1}}^{z_k}\left(\frac{\partial u}{\partial x}+\frac{\partial v}{\partial y}\right)\mathrm{d}z, \tag{2}$$

where $\omega(z)$ represents the vertical velocity at depth z, and u, v are the horizontal velocities at the corresponding depth. The depth variable is denoted by z. A surface boundary condition is applied by assuming zero vertical velocity at the sea surface, $\omega(z=0)=0$. Given that HYCOM provides isopycnic layer-based data, Eq.2 is further discretized into a layer-wise integral form, as shown below:

$$\omega(k)=\omega(k-1)-\Delta z\times\left(\frac{\partial u}{\partial x}+\frac{\partial v}{\partial y}\right)_{k-\frac{1}{2}}. \tag{3}$$

Here, Δz denotes the vertical layer thickness, and z_k represents the midpoint of the k layer. The term

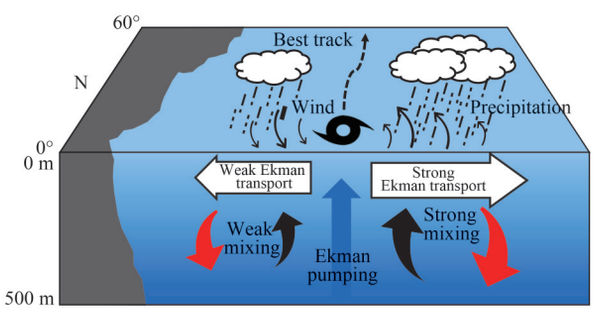

Fig.2 A schematic diagram of the upper ocean response to typhoons

$\left(\frac{\partial u}{\partial x}+\frac{\partial v}{\partial y}\right)_{k-\frac{1}{2}}$ refers to the average horizontal divergence between adjacent layers. Using Eq.3, the vertical velocity at different depths can be calculated accordingly.

3 TEMPORAL RESPONSE ANALYSIS BASED ON ARGO OBSERVATION

3.1 Salinity

The salinity profiles (Fig.3a, c, e, g) reveal a multi-phase dynamic adjustment of the salinity field in response to typhoon forcing. Prior to typhoon passage, sea surface salinity (SSS) remains relatively stable, exhibiting minimal perturbation from localized factors such as anomalous evaporation or heavy precipitation. The vertical salinity gradient is weak, and stratification maintains stable. However, pronounced salinity fluctuations emerged after typhoon passage, typically manifesting as a decreasing trend. For instance, during Typhoon Muifa in August–September 2022 (Fig.3c), SSS decreased by approximately 0.1–0.6 following the typhoon's transit, a response attributed largely to enhanced freshwater input from heavy typhoon-induced rainfall. Concurrently, the vertical salinity gradient weakened, and the mixed layer depth (MLD) thickened, underscoring the dominant role of wind-driven vertical mixing in restructuring the salinity distribution. Over the longer term, salinity recovery is modulated by a combination of oceanic and atmospheric processes, including advection by ocean currents, the evaporation-precipitation balance, and terrestrial freshwater discharge. Notably, salinity restoration generally proceeds more slowly than temperature recovery, reflecting its conservative behavior in marine systems.

From an ocean dynamical perspective, typhoon-associated intense precipitation directly reduces SSS, while wind-driven vertical mixing entrains low-salinity surface water with saltier subsurface water, weakening the vertical salinity gradient. Typhoon-induced upwelling and anomalous advection further modulate the salinity structure, as upwelling may elevate saline deep waters, counteracting precipitation-induced freshening and generating complex, non-linear salinity responses. Following typhoon passage, the ocean undergoes gradual adjustment through both internal dynamics (e.g., circulation restoration and stratification re-establishment) and external forcing (e.g., evaporation, precipitation and terrestrial freshwater input). Salinity recovery is

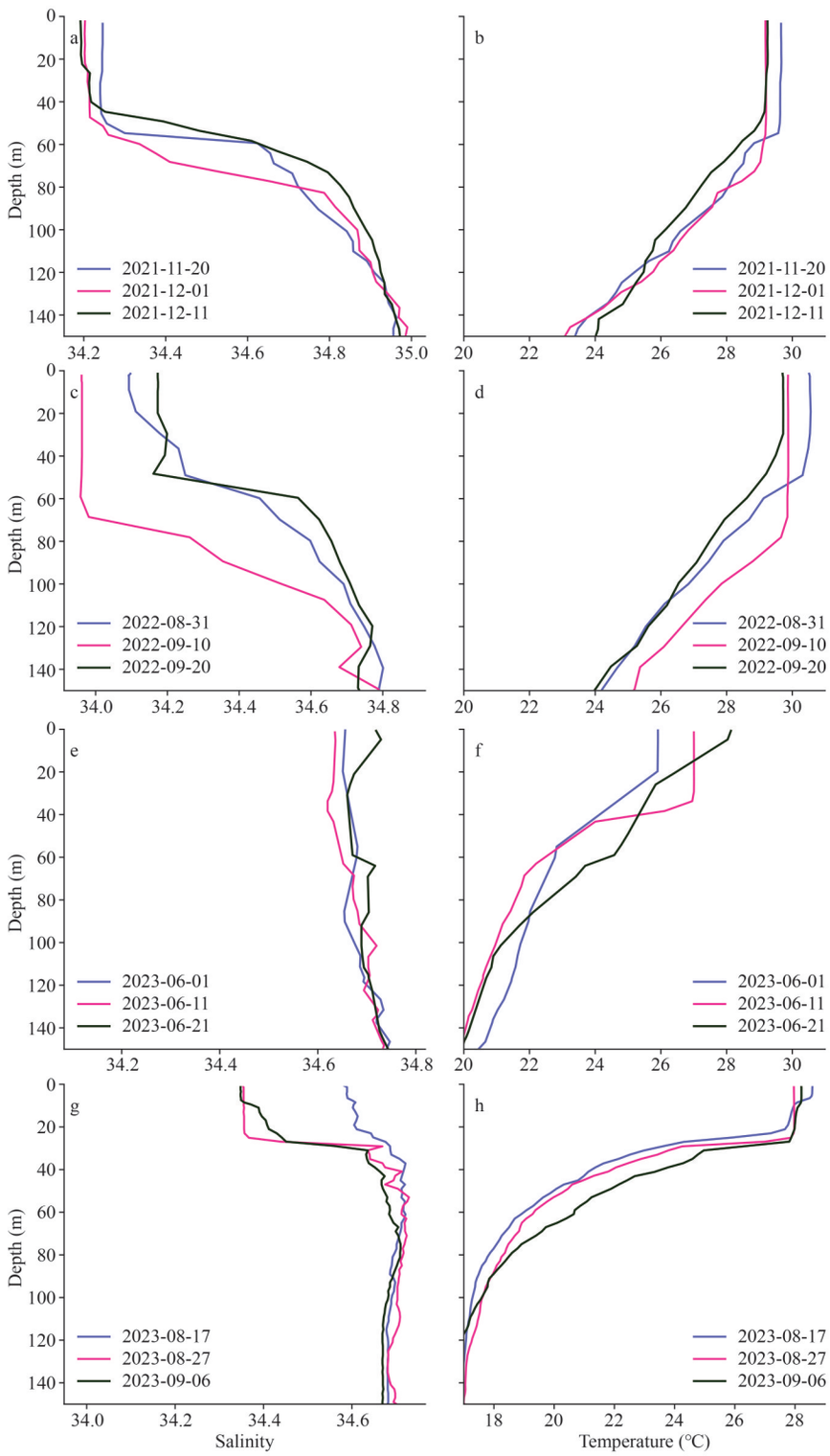

Fig.3 Contrast diagrams of Argo buoy temperature and salinity profiles before and after typhoon passage

Profiles in purple represent 10 d before passage, pink during passage, and dark green 10 d after passage. Panels (a–h) correspond to the profiles of typhoons Nyatoh (a, b), Muifa (c, d), Guchol (e, f), and Damrey (g, h), respectively.

mediated by advective transport and diffusive mixing, all constrained by the prevailing large-scale ocean circulation. For example, by early September (Fig.3g), the salinity profile had not yet reverted to pre-typhoon conditions, reflecting the delayed restoration timescale characteristic of salinity fields.

3.2 Temperature

Figure 3b, d, f, & h clearly demonstrates the dynamic thermal evolution of the upper ocean in response to typhoon passage. Prior to typhoon passage, the upper ocean exhibited distinct thermal stratification, with warmer surface water and a strong temperature gradient at the MLD indicating a stable shortwave radiation driven structure. During typhoon passage, SST experienced an abrupt decrease, forming the typhoon cold wake phenomenon (Zhang et al., 2019a; Yu et al., 2023). This cooling was resulted from wind-driven vertical mixing that entrained colder subsurface waters, showing homogenization and reduced gradients from the surface down to 50–100 m. In the subsequent recovery phase (~10-d post-typhoon), the upper ocean exhibited gradual thermal readjustment. Due to slow heat recovery, surface temperatures remained lower than pre-typhoon levels. MLD decreased but maintained greater thickness than pre-storm conditions. Comparing among cases, the post-typhoon recovery rate of seawater temperature was notably slower than the rate of initial perturbation, reflecting a nonlinear ocean thermal response to typhoon forcing.

During typhoon passage, wind-driven Ekman pumping and enhanced vertical mixing fundamentally modified the vertical stratification structure. This is clearly evidenced by the Argo profiles (Fig.3), where the post-typhoon temperature curves show surface cooling and a homogenized layer extending much deeper than the pre-typhoon profiles. In offshore regions, vertical turbulent mixing became the dominant mechanism governing momentum and heat exchange between the surface and subsurface layers. This process induced notable surface cooling through two complementary mechanisms, which are direct upwelling of colder deep waters and wind-driven entrainment across the mixed layer base, with the abrupt deepening of the mixed layer serving as a clear indicator of mixing intensity. The post-typhoon thermal recovery phase is primarily driven by surface heat flux through solar shortwave radiation absorption and horizontal advective heat transport from adjacent warmer waters. From a dynamical perspective, this recovery represents a gradual re-establishment of quasi-equilibrium thermocline structure, with its timescale being determined by the competing effects of local advection-diffusion processes and incident solar radiation flux. Notably, the ocean thermal field exhibits pronounced hysteresis in its response to typhoon forcing, as the 10-d post-typhoon temperature profiles in Fig.3 have not yet returned to their pre-typhoon states, indicating a longer recovery timescale than the observation window.

3.3 Mixed layer depth

After typhoon passage, both temperature and salinity profiles exhibited a substantial increase in uniform layer thickness, demonstrating significant MLD deepening. In Typhoon Nyatoh, the MLD deepened from 51.70 to 55.40 m following typhoon passage, while Typhoon Muifa showed an increase from 29.30 to 72.10 m, and Typhoon Damrey deepened from 20.40 to 32.90 m. As clearly shown in typhoon Guchol's profiles (Fig.3e & f), the MLD experienced progressive expansion over several days post-typhoon. Enhanced wind-driven mixing in the upper ocean, fueled by the typhoon's strong wind stress, disrupted the stable stratification, and deepened the MLD. The temperature profile exhibited an increased thickness of the cool surface layer, while the salinity profile showed an expanded mixed layer. This process aligns with mixed layer theory (e.g., the Munk-Anderson model), where wind stress drives mixed layer vertical development through turbulent kinetic energy generation.

During the subsequent re-stratification phase, the upper ocean gradually recovered its mixed layer thickness. The Argo observations clearly captured this recovery pattern across all cases. In Typhoon Nyatoh, the MLD recovered to 40.10 m in 10 d; Typhoon Muifa returned to 39.60 m; and Typhoon Damrey stabilized at 29.40 m. This occurred via solar radiation heating the surface, re-establishing a temperature gradient, and stabilization under weaker winds. The recovery speed is closely linked to ocean environmental parameters, such as the thickness of the warm water layer and the background buoyancy frequency. Regions with a thicker warm layer and lower buoyancy frequency experienced relatively faster mixed layer recovery, reflecting the coupled adjustment of oceanic dynamic and thermal processes.

4 SPATIAL RESPONSE

4.1 HYCOM validation

To investigate the spatial response of the upper ocean to typhoons, HYCOM reanalysis data were used. Prior to spatial analysis, a comprehensive validation of HYCOM performance was conducted

against Argo observations. As quantitatively demonstrated by the basin-averaged RMSE and correlation coefficients across the four typhoon cases, HYCOM exhibits distinct performance characteristics for temperature and salinity simulations during different typhoon phases.

We computed the correlation coefficients between the HYCOM and Argo along the profiles. Since the depth layers of HYCOM and Argo do not coincide, linear interpolation was applied to map the HYCOM salinity and temperature data onto the exact depth levels of each Argo profile, ensuring data alignment. Subsequently, for each matched time point (pre, transit, and post), the profile of Argo-observed salinity (temperature) and the corresponding interpolated HYCOM-simulated profile were treated as a paired sample. Then the Pearson correlation coefficient between these two sequences was calculated to quantitatively assess the ability of the HYCOM model and to reproduce the observed vertical structure.

Correlation analysis demonstrates HYCOM's strong capability in reproducing observed temporal variations (Fig.4). For temperature, remarkably high correlations were maintained across all phases (pre: 0.996 8±0.004 0; transit: 0.997 1±0.002 5; post: 0.998 1±0.001 1), indicating excellent consistency in capturing thermal evolution trends. Salinity correlations were also substantial, though with greater variability among cases, particularly during the transit phase where Typhoon Muifa showed reduced correlation (0.790), resulting in a lower average (0.916 6±0.074 3) compared to pre- (0.964 9±0.017 0) and post-typhoon (0.962 0±0.018 9) phases. This pattern reflects the challenges in simulating salinity under strong precipitation and mixing conditions during active typhoon forcing.

Error analysis reveals systematic model biases that complement the correlation patterns shown in Fig.5. For salinity, the Root Mean Square Error (RMSE) remains relatively stable with depth (generally below 0.15), with slightly higher values during transit within 100-m depth. This consistency with profile comparisons suggests adequate representation of the surface layer but a gradual decline in accuracy at greater depths. The temperature validation reveals more pronounced quantitative discrepancies. Despite high correlations, RMSE peaks in the upper layers (0.8–1.0 °C) during transit and post-typhoon period, particularly within the critical mixing layer above 100-m depth. This substantial warming bias indicates that while HYCOM reproduces the temporal variation of temperature well, it systematically underestimates the intensity of vertical mixing. Below 150 m, temperature RMSE decreases to 0.4–0.8 °C across all periods, indicating a better performance in deeper layers where typhoon-induced variations are minimal.

The integrated analysis demonstrates that HYCOM consistently reproduces observed thermohaline trends with high fidelity (correlations >

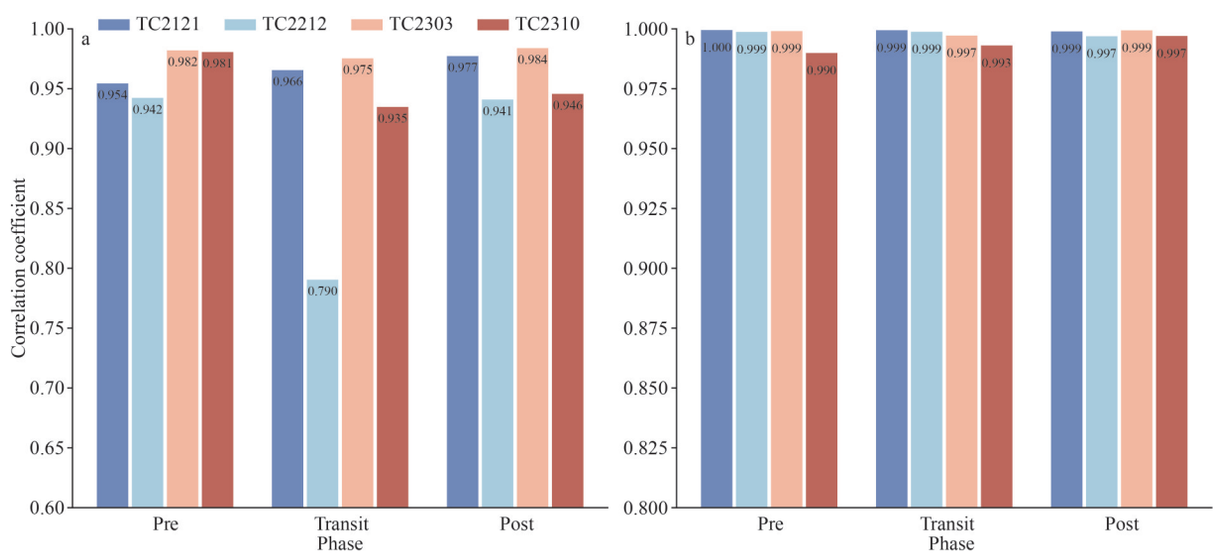

Fig.4 Correlation coefficients between HYCOM model data and Argo observations for pre, transit, and post of four typhoon cases

a. salinity correlation coefficients; b. temperature correlation coefficients. Dark blue for Typhoon Nyatoh (TC2121), light blue for Typhoon Muifa (TC2212), pink for Typhoon Guchol (TC2303), and red for Typhoon Damrey (TC2310).

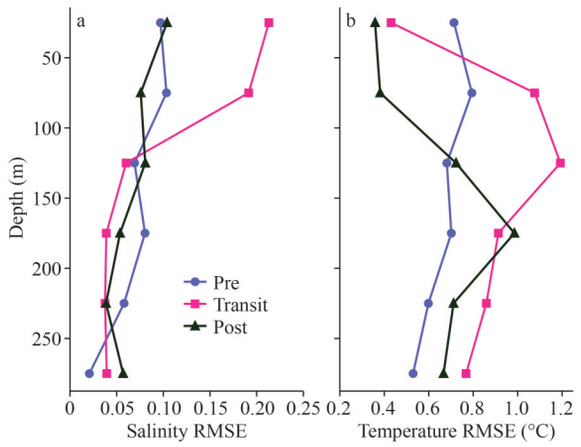

Fig.5 Root Mean Square Error (RMSE) between HYCOM model data and Argo observations before, during, and after the passage of four typhoon cases

a salinity RMSE; b. temperature RMSE. Colors indicate different phases: purple for pre-typhoon, pink for during typhoon passage, and dark green for post-typhoon.

0.9), but systematically underestimates key physical processes. This is evidenced by a marked bias in temperature during active typhoon conditions, despite its excellent pattern reproduction.

During typhoon passage, both datasets captured the characteristic homogenization of mixed layer salinity and cooling, but Argo data exhibited a more significant SSS decrease and cooling than HYCOM. This discrepancy may stem from insufficient model representation of dilution by precipitation and the intensity of wind-driven vertical mixing. Ten days after typhoon passage, Argo data indicate gradual recovery of salinity and temperature, while HYCOM recovery lags, reflecting delayed model response to ocean dynamical adjustment and heat recovery processes. For Typhoon Muifa (Fig.6c–d), Argo data show a marked SSS drop during passage (down to 34). HYCOM captures the homogenization trend but underestimates the decrease and exhibits an erroneous inverse salinity response under typhoon forcing, highlighting limitations in simulating intense precipitation dilution dynamics.

Furthermore, the Argo-derived salinity-homogeneous layer extends deeper than that in HYCOM, suggesting potential deficiencies in the model's vertical mixing parameterization. Figure 6e & f reveals that HYCOM produces smoother deep salinity profiles compared to the finer-scale fluctuations observed in Argo data, suggesting the model's limited capacity to resolve small-scale salinity variations. After typhoon passage, HYCOM salinity recovery broadly follows the Argo trend but exhibits persistent biases, implying potential inaccuracies in simulating freshwater input or open-ocean advection processes. suggesting errors in simulating freshwater input or open-ocean advection. Additionally, HYCOM's slower temperature recovery rate relative to Argo may result from an inadequate representation of oceanic heat advection, leading to a failure in capturing the observed post-typhoon recovery lag. Regarding Typhoon Damrey (Fig.6g & h), Argo salinity during passage is significantly lower than pre-typhoon levels (due to precipitation), while HYCOM shows a slight underestimation. This may be attributed to model biases in simulating vertical mixing and long-term evaporation-precipitation balance. The vertical temperature gradient at the mixed layer base is weaker in HYCOM than that in Argo data, indicating weaker simulated stratification stability, stemming likely from inherent limitations in the turbulence closure scheme. Overall, the HYCOM data can capture mixed layer property trends and be used to further investigate the spatial response of upper ocean to typhoons.

4.2 Surface response

Typhoons, as extreme events of air-sea interaction, trigger rapid transient responses in the upper ocean's temperature and salinity structure during their passage—processes that are central to the redistribution of energy and materials within the oceanic boundary layer. As shown in panels (d) of Figs.7, 8, & 10, SST generally exhibits a significant cooling trend during typhoon passage compared to pre-typhoon conditions, with a temperature drop of 1–3 °C.

By examining the typhoon track (Fig.1b), it is observed that the cooling magnitude and salinity changes in the surface ocean differ on either side of the typhoon track. The typhoon-induced changes in SST and SSS exhibit a clear spatial asymmetry, with more pronounced variations occurring typically on the right side of the typhoon track. As shown in Figs.7, 9, & 10a, this asymmetry can be attributed to the uneven wind field associated with the typhoon, where stronger winds are generally present on the right side (Wang et al., 2022). The ocean response exhibits a pronounced rightward bias relative to the typhoon track. This asymmetry is primarily driven by the resonant coupling between the clockwise-

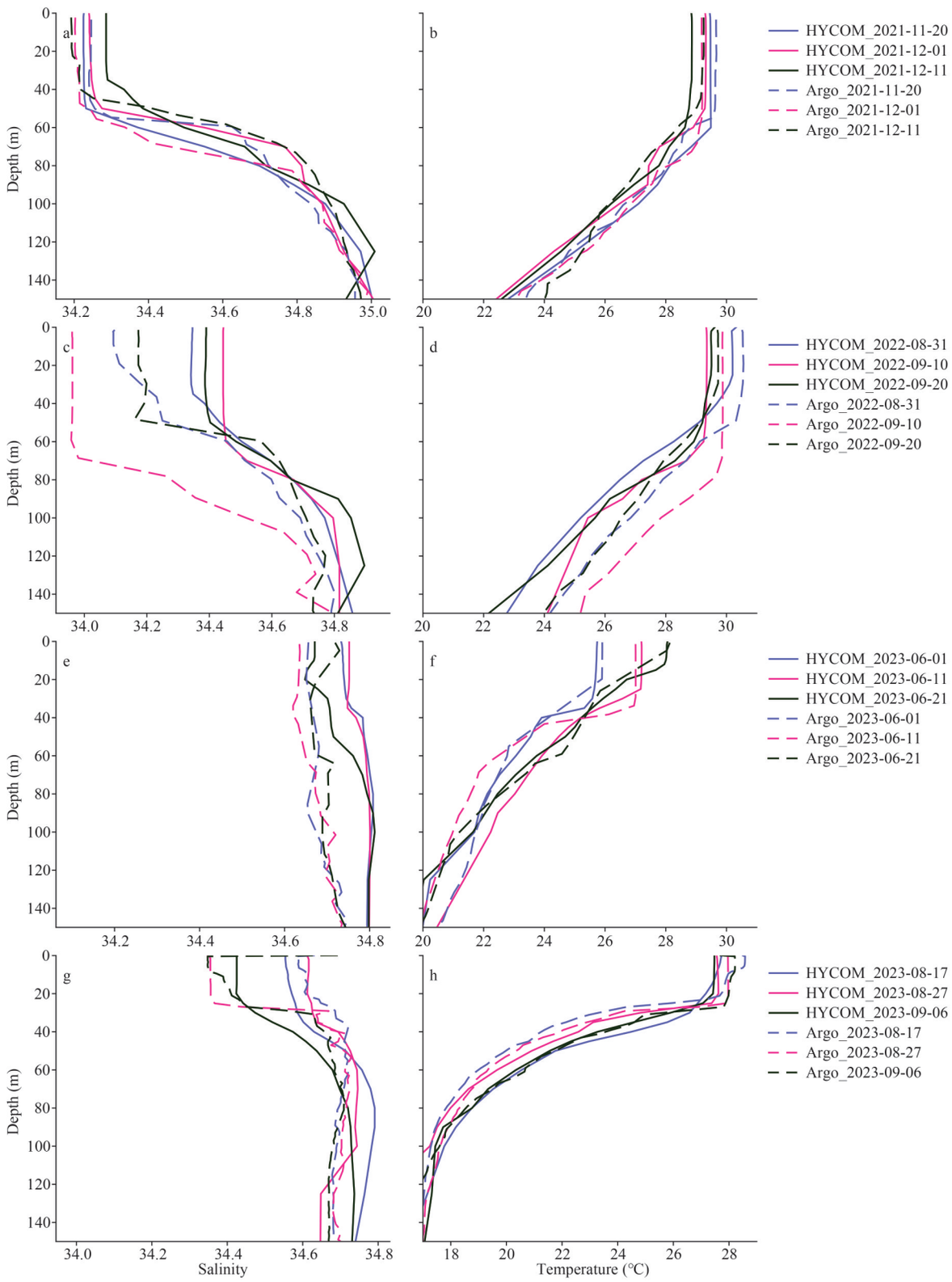

Fig.6 Comparative diagrams of temperature and salinity profiles from Argo observational data and HYCOM model data before and after typhoon passage

Profiles are shown for 10 d before passage (blue), during passage (pink), and 10 d after passage (green). Solid lines represent HYCOM model data, dashed lines represent Argo observational data. Panels (a–h) correspond to the temperature and salinity profiles for typhoons Nyatoh (a, b), Muifa (c, d), Guchol (e, f), and Damrey (g, h), respectively.

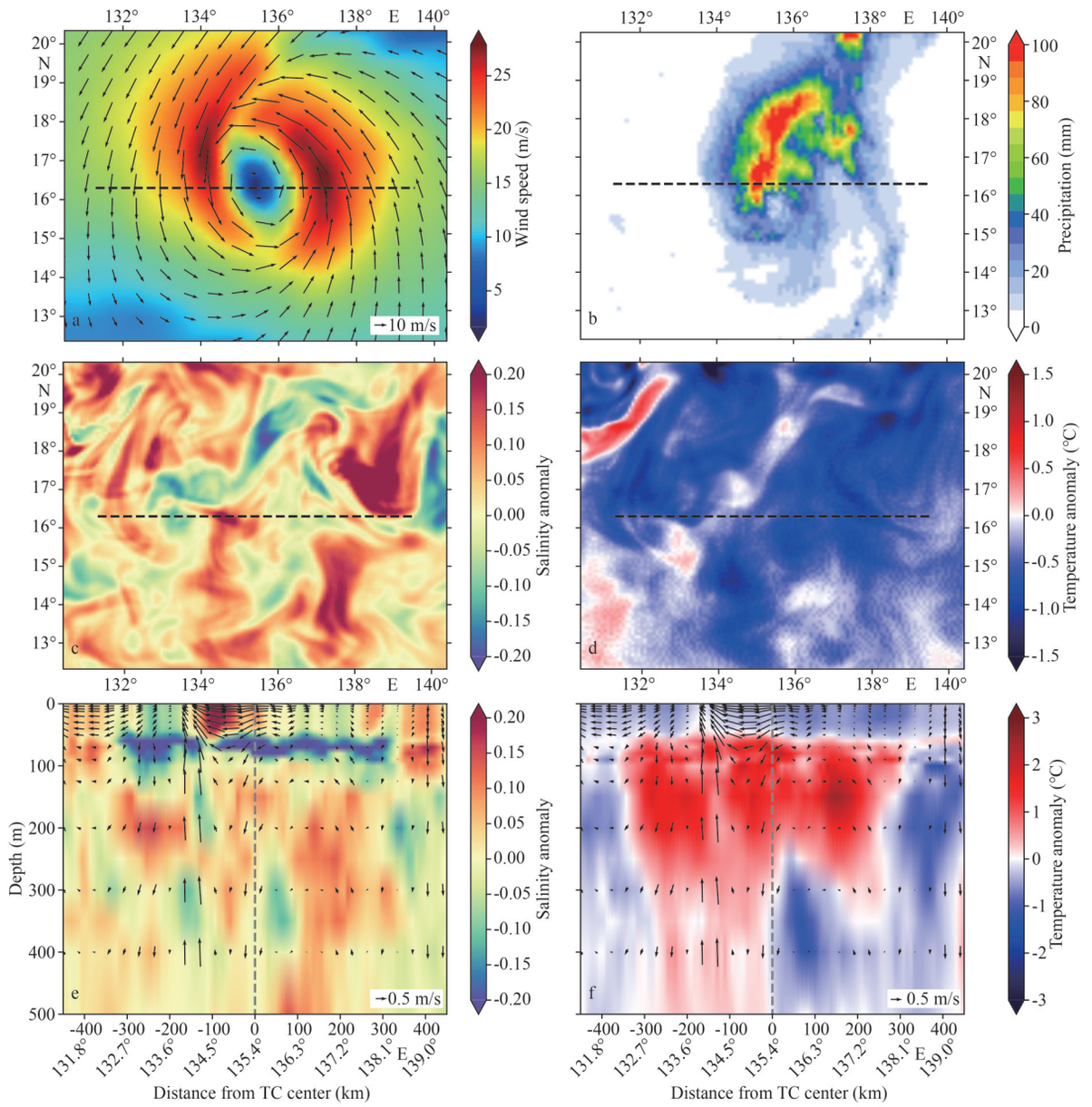

Fig.7 Analysis of multi-parameter ocean-atmosphere coupled observations during Tythoon Nyatoh

a. 10-m wind field at the sea surface (wind vectors, m/s); b. accumulated precipitation within three hours before typhoon passage; c. sea surface salinity anomaly; d. sea surface temperature anomaly; e. meridional section of salinity anomaly along the black dashed line shown in the figures; f. vertical structure of temperature anomaly along the corresponding latitude band. In panels (a–d), the black dashed lines indicate the location of the cross-section perpendicular to the typhoon track. In panels (e–f), the central gray dashed lines mark the typhoon center, and the arrows represent the composite vectors of vertical velocity (multiplied by 3) and horizontal velocity at the cross-section. TC: typhoon.

turning wind stress vector and the near-inertial currents in the mixed layer on the right side, which generates stronger currents and, consequently, more intense entrainment mixing and SST cooling in that region (Price, 1981).

4.3 Subsurface response

As the uppermost layer of the ocean, the mixed layer plays a critical role as the primary interface for air-sea interactions, mediating the exchange of heat, momentum, and mass between the atmosphere and the subsurface ocean. Variations in mixed layer depth significantly influence the vertical thermohaline structure of the water column. During typhoon passage, the combined effects of intense wind forcing and surface cooling generate turbulent

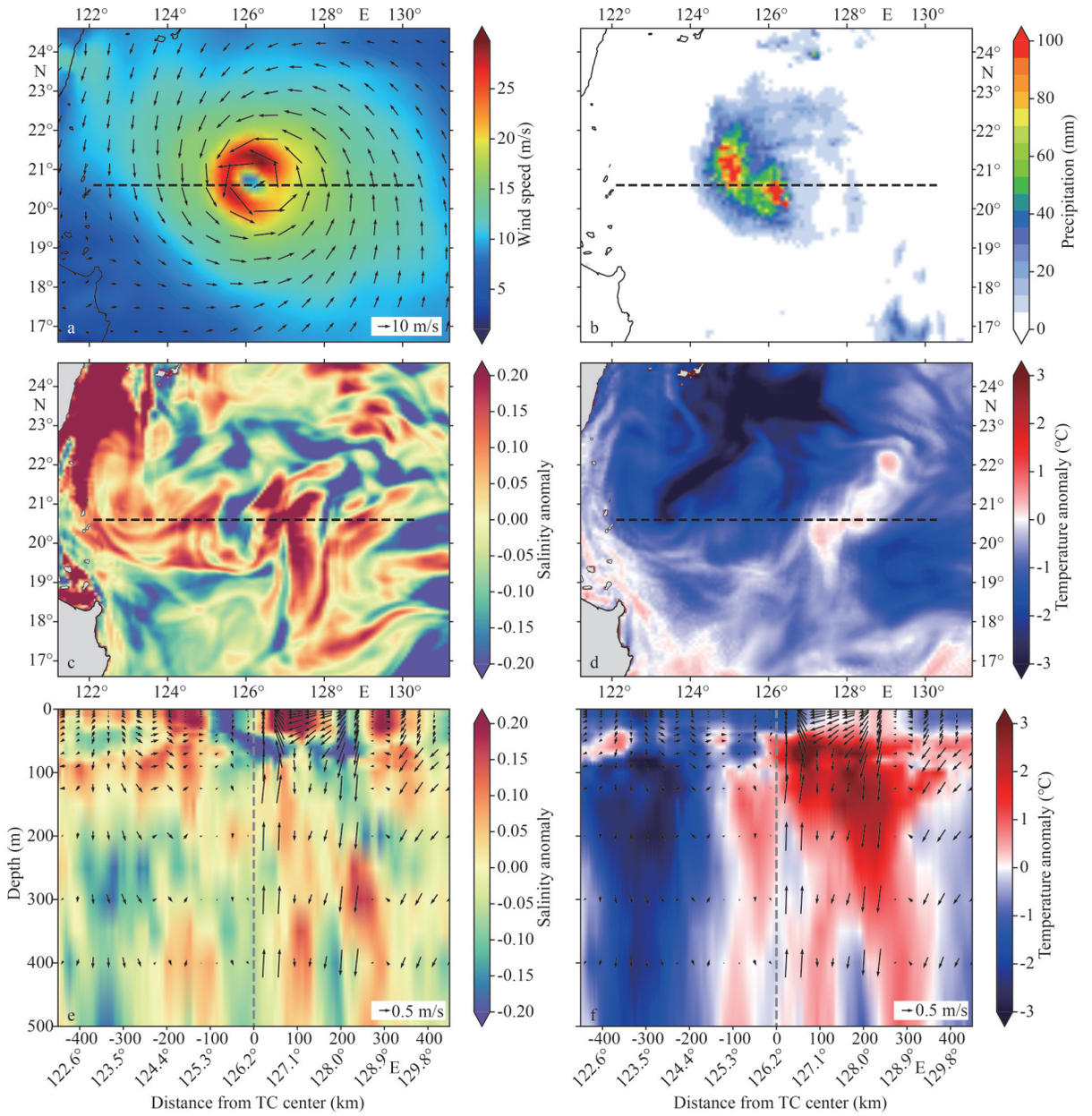

Fig.8 Same as in Fig.7, comprehensive analysis of multi-parameter ocean-atmosphere coupled observations during Typhoon Muifa

mixing that penetrates the pycnocline, entraining deeper waters, and causing substantial deepening of the mixed layer. This wind-driven mixing process effectively redistributes surface properties downward, altering the underlying stratification. Given that all selected typhoons followed generally northward-moving tracks, we specifically analyzed zonal cross sections. It enables a clearer investigation of the cross-track asymmetry in upper ocean responses, with pronounced responses on the right side and weaker responses on the left side relative to the storm's movement direction.

As shown in panels (e–f) of Figs.8–10, the homogenized layers of salinity and temperature can be clearly observed to extend down to depths of 500 m below the ocean surface during typhoon events, indicating a deepening of the oceanic mixed layer into the subsurface region. Such a response is consistent with the deepening of the mixed layer observed in the temperature and salinity profiles derived from Argo buoy observation before and after typhoon passage, thereby confirming the

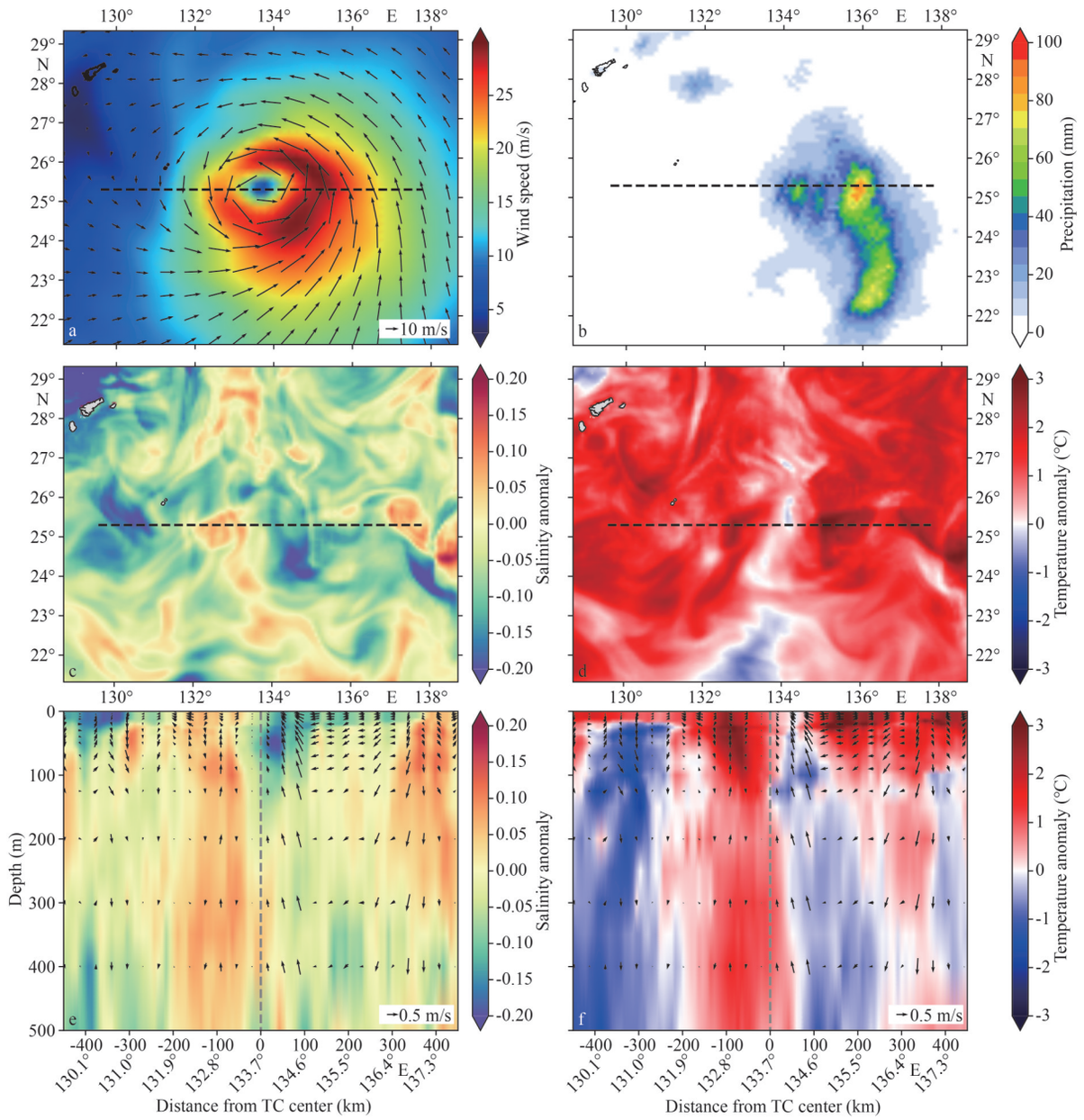

Fig.9 Same as in Fig.7, comprehensive analysis of multi-parameter ocean-atmosphere coupled observations during Typhoon Guchol

subsurface ocean's dynamic response to typhoons. This enhanced vertical mixing facilitates intensified heat and mass transfer between surface and subsurface layers, ultimately modifying the thermohaline structure of the water column. It is noteworthy that this vertical redistribution of energy, predominantly driven by mixing, often results in a characteristic multi-layered thermal structure. The pronounced subsurface temperature anomalies (80–500 m) observed in multiple cases of this study (Figs.7–10) are consistent with the complex vertical structure previously identified in typhoon wake studies. Such a structure typically manifests as near-surface cooling underlain by warming, accompanied by dipole anomalies within the thermocline, collectively forming a classic four-layer thermal response of the upper ocean to typhoon forcing (Pei et al., 2015).

4.4 Thermodynamic and dynamic influence

4.4.1 Precipitation

Precipitation is one of the major factors influencing SSS during typhoon events and is closely associated with salinity changes in space.

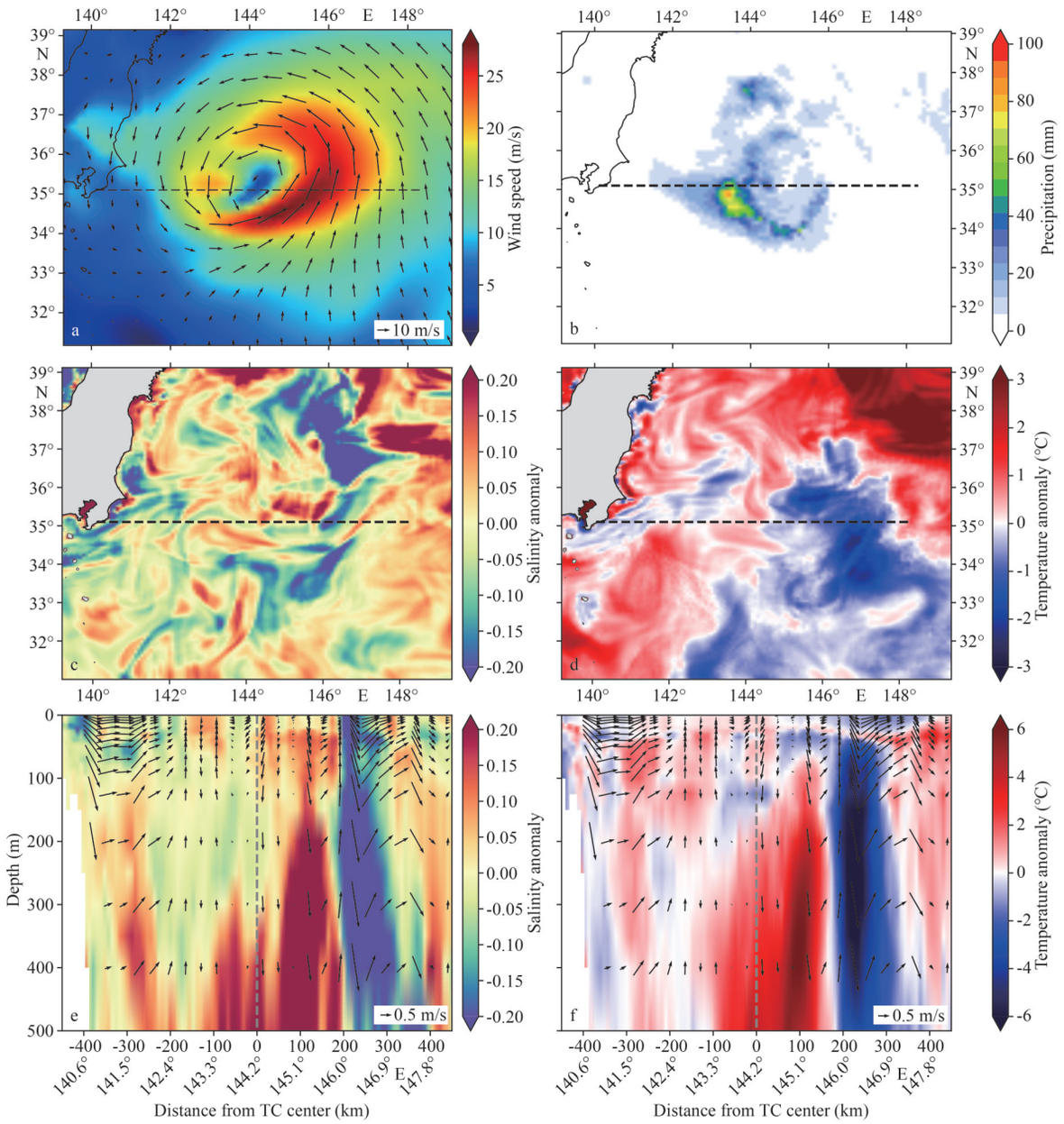

Fig.10 Same as in Fig.7, comprehensive analysis of multi-parameter ocean-atmosphere coupled observations during TC Damrey

The substantial freshwater input from typhoon-induced rainfall creates pronounced surface dilution, as clearly seen in Fig.7e showing the characteristic vertical salinity gradient. By combining the SSS distribution (Fig.7c) with the accumulated precipitation in the three hours before typhoon hit (Fig.7b), we can see clearly that the upwelling of high-salinity water from deeper layers compensated the freshening effect of rainfall. The net salinity response demonstrates spatial dependence, with precipitation-dominated areas showing clear surface freshening, confirming that rainfall dilution remains the predominant control on SSS variations during typhoon conditions. The salinity anomaly cross-sections (Figs.7e & 8e) reveal a distinct low-salinity layer within the upper 100 m of the water column. This freshwater lens, generated by precipitation input, creates a negative salinity anomaly in the surface layer. However, the concurrent presence of subsurface warming alongside salinity reduction in the vertical profiles indicates that vertical mixing, rather than precipitation-induced freshening, acts as

the dominant process regulating the upper ocean thermalhaline structure during typhoon passage. The entrainment of warmer and saltier subsurface waters through wind-driven mixing effectively counteracts and masks the localized surface freshening signal, resulting in the observed warming trend with salinity decrease in the subsurface layer. Meanwhile, the underlying water mass maintains its higher density characteristics, resulting in an intensified density gradient across the pycnocline. This enhanced stratification effectively inhibits vertical mixing processes, thereby exerting substantial influence on both the ocean's stratification and associated dynamic processes. Typhoon precipitation exhibits fundamentally different spatial characteristics from conventional convective rainfall, displaying pronounced heterogeneity in its distribution.

Precipitation tends to be lighter near typhoon center and heavier in the surrounding rainbands outside the eyewall. The accumulated precipitation profiles (panels (c) in Figs.7–10) clearly show uneven rainfall distribution in the typhoon-affected regions where SSS was notably reduced in the areas of heavier rainfall. Figures 9–10, which correspond to typhoons Guchol and Damrey respectively, demonstrate that in peripheral areas of heavy rainfall, SSS is significantly lower than in the typhoon center, where less rainfall but stronger wind-induced mixing occurs. These spatial variations in precipitation create horizontal salinity gradients, which can induce density differences and, consequently, horizontal ocean currents. These flows affect the transport of materials and energy in the ocean and further complicate the spatial distribution of SSS.

Precipitation also has a certain impact on SST, generally acting to weaken surface cooling. By comparing precipitation regions and surface temperature anomalies in Figs.7, 8, & 10, it is evident that in regions with heavier rainfall, the overall cooling trend is noticeably weaker, and in some cases, a warming tendency is observed. This is primarily attributed to the formation of a barrier layer or enhanced near-surface stratification by freshwater input, which suppresses vertical mixing and entrainment of colder subsurface waters, thereby dampening the SST decrease (Krishnamohan et al., 2019). Recent research further demonstrates that the freshwater flux forcing (warming) induced by precipitation and the wind stress forcing (cooling) exhibit a direct competitive relationship in governing SST; when precipitation is sufficiently strong (e.g., >10.37 mm/h), the surface warming effect driven by freshwater input can even surpass the wind-driven cooling effect (Ye et al., 2023). However, this moderating effect is not uniform across all cases or even within a single storm, as it critically depends on the relative intensity of these competing forcings. The impact on SST alters heat exchange between the ocean and atmosphere, which in turn influences the development and maintenance of typhoon. Weaker surface cooling implies greater heat flux into the atmosphere, favoring the sustenance of the typhoon's intensity.

4.4.2 Vertical mixing and Ekman transport

Under the influence of typhoon, strong wind stress and waves significantly enhance vertical mixing in the upper ocean. The spatial pattern of this mixing is largely governed by the wind stress curl distribution (Fig.11), which drives divergent Ekman transport and initiates Ekman pumping. This mixing process facilitates the exchange between warm surface water and cooler subsurface water, transferring heat from the surface to deeper layers and thereby altering the ocean's temperature structure. Figures 7–10 illustrate that for the four typhoon cases, the upper ocean exhibited temperature anomalies with warming of more than 3 °C at depths between 80 and 500 m after typhoon passage. Notably, during Typhoon Damrey, an upwelling region with cooling exceeding 6 °C formed within the vertical water flow pathway driven by Ekman suction, accompanied by a corresponding downwelling region with temperature increases of around 6 °C. Further analysis of the Richardson number (*Ri*) within the 50-m mixed layer (Fig.12) revealed values frequently falling below the critical threshold of 0.25 in these regions of strong vertical flow, indicating suppressed stratification and enhanced turbulent mixing conditions. Analysis of water movement along the cross-section reveals that the upwelling of cold high-salinity water from the subsurface mixes with warm low-salinity surface water, resulting in surface temperature decreases and salinity increases.

The Ekman pumping induced by typhoons alters the ocean structure through vertical water transport, while its associated horizontal motion drives cross-density material fluxes. Quantitative analysis of the wind stress curl fields demonstrates pronounced spatial heterogeneity, with maximum values

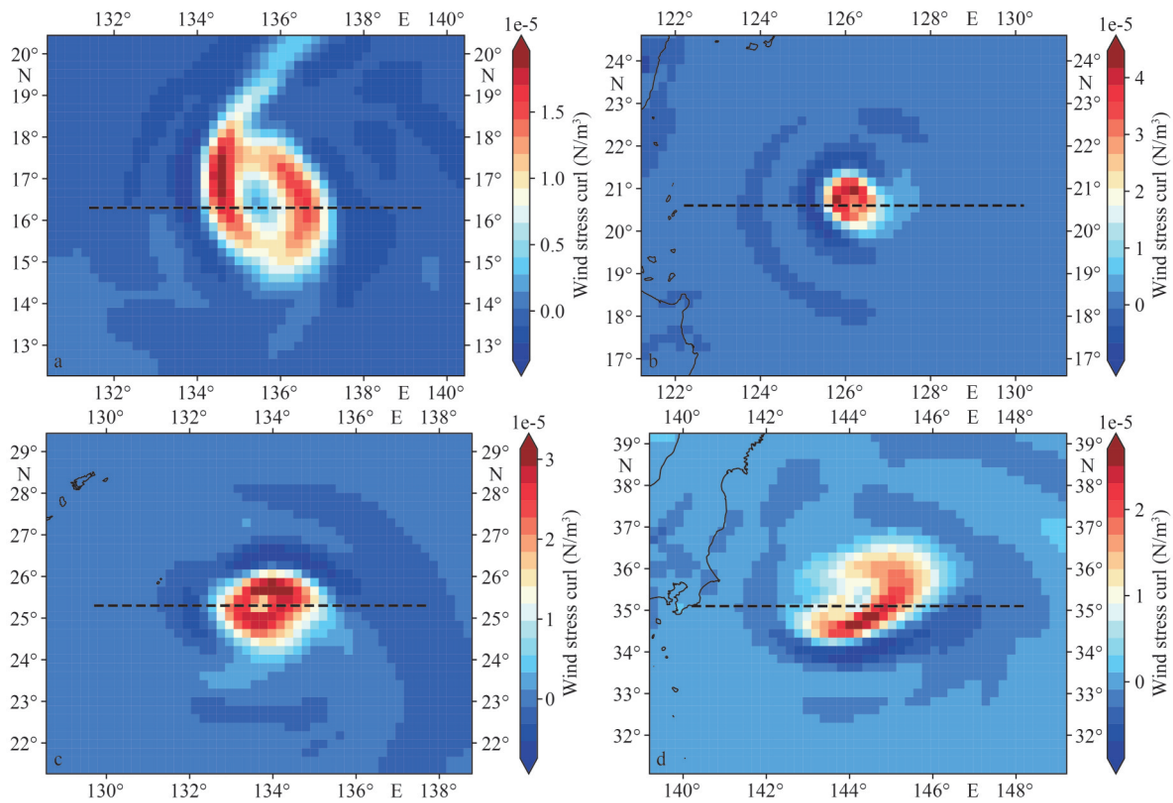

Fig.11 Wind stress curl for the four typhoon cases

a. Typhoon Nyatoh; b. Typhoon Muifa; c. Typhoon Guchol; d. Typhoon Damrey. The black dashed lines indicate the location of the cross-section perpendicular to the typhoon track.

concentrated near the typhoon center and extending along the right side of the track. The direction and intensity of Ekman pumping and transport vary across different ocean regions, influencing the redistribution of heat and salinity. Notably, there are marked differences in Ekman pumping between the typhoon center and its periphery. Near the typhoon center, stronger wind stress and wave action intensify vertical mixing in the upper ocean, which homogenizes the water column and entrains water from below, leading to mixed layer deepening and surface cooling. The corresponding reduction in *Ri* values within the 50-m mixed layer to below 0.25 confirms the dominance of shear production over buoyancy effects in these regions, facilitating the observed mixed layer deepening, which results in a deeper mixed layer and more pronounced temperature changes. In contrast, at the typhoon's outer regions, Ekman-induced vertical mixing is relatively weaker, with smaller changes in MLD and temperature. Consequently, the ocean's physical properties within the typhoon-affected area display spatial heterogeneity, which in turn feeds back to influence the typhoon's track and intensity evolution.

Ekman pumping disrupts the original ocean stratification by changing the position and strength of the thermocline. A previously stable thermocline may be weakened or displaced downward, affecting the vertical distribution of heat, salinity, and nutrients within the ocean. As shown in the temperature and salinity profiles in Fig.3, under typhoon influence, Ekman pumping causes vertical displacement of the thermocline, thereby altering the local vertical temperature gradient, facilitating downward heat transfer and resulting in warming of subsurface waters. This destratification process is quantitatively supported by the observed decrease in *Ri* values within the upper water column, particularly within the 50-m mixed layer where *Ri* frequently dropped below 0.25 during peak forcing conditions. This phenomenon aligns with the vertical mixing processes described earlier in this section.

Furthermore, Ekman transport drives horizontal water movement, enabling material transport across the ocean surface. In the upper 100 m of the vertical sections presented in Figs.7–10, the surface water

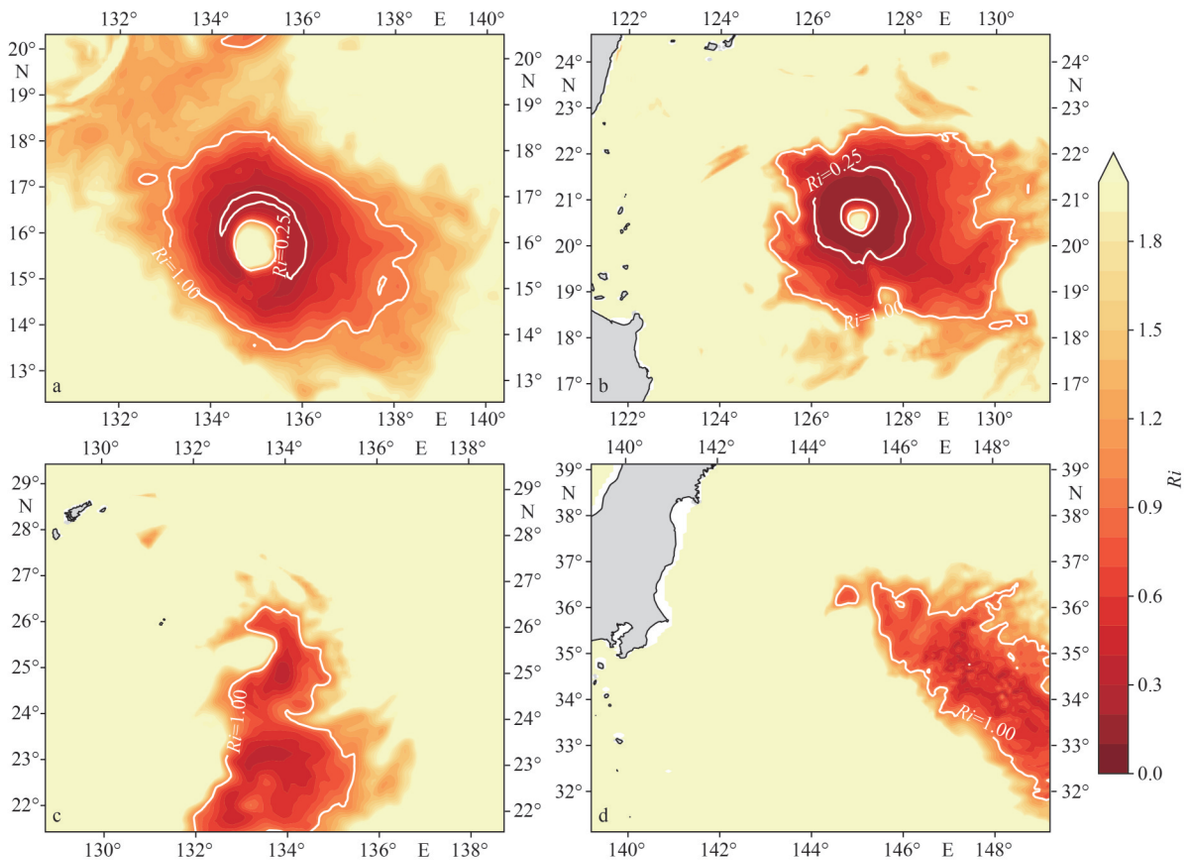

Fig.12 The Richardson number (*Ri*) in the 50-m mixed layer

a. Typhoon Nyatoh; b. Typhoon Muifa; c. Typhoon Guchol; d. Typhoon Damrey.

flow direction shows that under typhoon forcing, Ekman transport would cause surface waters to accumulate on the outer side of the typhoon track, inducing compensatory upwelling at the typhoon center and downwelling where waters accumulate at the periphery. This circulation pattern forms the characteristic Ekman suction. Meanwhile, as the typhoon moves, heat, salinity, nutrients, pollutants, and other substances are redistributed across different ocean regions by Ekman transport, playing a vital role in the global balance of heat and salinity.

5 DISCUSSION AND CONCLUSION

The response of the upper ocean to typhoons is a complex process involving multiple oceanic elements—such as temperature, salinity, and mixed layer depth—driven by the combined effects of oceanic dynamical and thermodynamical processes. As the initial driving force, typhoon-induced strong wind stress deepens the mixed layer, disrupts the stratification of temperature and salinity, promotes vertical homogenization of temperature, and induces salinity adjustment. Temperature responds rapidly through dynamic mixing and air-sea heat exchange, while salinity distribution is adjusted by freshwater input from precipitation and mixing processes. The mixed layer depth expands in response to increased energy input. After typhoon passage, the ocean gradually recovers through thermodynamic processes such as solar shortwave radiation and internal heat redistribution, as well as dynamical processes like circulation recovery and stratification re-stabilization. Due to different physical properties of oceanic variables, their recovery patterns vary.

This study focuses on the response mechanisms of the upper ocean to typhoons in the northwest Pacific. Based on Argo buoy observations, HYCOM reanalysis data, and multi-source observational datasets from four representative typhoons between 2021 and 2024, this investigation was conducted systematically on the typhoon-induced variations in thermohaline structure, mixed layer depth, and oceanic dynamic processes through comprehensive temporal and spatial analyses. The principal conclusions are summarized as follows:

(1) After typhoon passage, SST dropped significantly by 1.5–6 °C, salinity decreased by 0.1–0.6, and the mixed layer depth increased from 50 m to 100–150 m, reflecting the effects of wind-driven vertical mixing and freshwater dilution from precipitation. Temperature profiles indicate homogenization between surface and subsurface cold water, while salinity profiles show reduced gradients due to the combined effects of precipitation and mixing. Notably, the recovery rates of temperature and salinity differ significantly: temperature gradually rises within 10 d through solar radiation and horizontal advection, whereas salinity, due to its conservative nature and influence from terrestrial inputs, takes longer to recover. The mixed layer depth decreases over time as stratification stabilizes but remains higher than pre-typhoon levels, indicating the nonlinear temporal response of ocean dynamical-thermal processes. In the Northern Hemisphere, cooling, freshening, and mixed layer deepening are more pronounced on the right side of the typhoon track, associated with stronger wind stress and intensified Ekman suction and vertical mixing. Vertical mixing extended down to 500 m, redistributing subsurface thermohaline structures via convective and advective processes. HYCOM data reveal more than 3 °C warming in downwelling regions and over 6 °C cooling in upwelling regions between 80–500 m, highlighting the critical role of Ekman suction in subsurface energy redistribution.

(2) Comparisons between numerical simulations and in-situ observations indicate that the HYCOM model can generally capture trends of mixed layer deepening, SSS reduction, and SST decline under typhoon influence. However, discrepancies remain in the magnitude, variability, and detailed characteristics. The model underestimates the dilution effect of intense precipitation and the variability in deep salinity. Additionally, simulated temperature changes show biases in cooling magnitude, recovery rate, and stratification gradients. These differences likely stem from limitations in parameterization schemes, such as vertical mixing, precipitation processes, model resolution, or inaccuracies in initial and boundary conditions.

(3) The upper ocean thermohaline responses to typhoon are driven by the combined effects of dynamic processes (e.g., Ekman pumping, near-inertial currents) and thermal processes (e.g., latent heat release, precipitation input). In this study, we found that vertical mixing contributes more to SST reduction than direct cooling from precipitation (Yang et al., 2019a), confirming that wind-driven upwelling of deep cold water is the primary mechanism behind the formation of “cold wakes”. Salinity changes are governed by both precipitation-induced freshwater dilution and upwelling of high-salinity deep water. For instance, in the Typhoon Kujira case, salinity increased by up to 0.5 in upwelling regions, which partially offset the dilution effect of rainfall, revealing the complexity of internal oceanic material transport.

(4) The asymmetry of typhoon wind fields is a major factor in the spatial heterogeneity of ocean responses. In the Northern Hemisphere, stronger winds on the right side of the typhoon path enhance Ekman transport and drive stronger vertical motion. For example, in Typhoon Muifa, the downwelling velocity on the right side reached 0.05 m/s, compared to just 0.03 m/s on the left. Furthermore, mesoscale eddies, such as warm-core eddies, can delay mixed layer deepening, while cold-core eddies accelerate energy dissipation. Coastal topography also enhances tidal mixing, further influencing response intensity. In Typhoon Lekima, nearshore SST cooling reached 6 °C, being significantly higher than the 2.5 °C observed offshore, directly linked to enhanced vertical mixing due to tidal effects (Liu et al., 2022).

On the other hand, there are several limitations that warrant discussion. The HYCOM model simulations show limited accuracy in capturing detailed typhoon tracks and upper ocean thermohaline responses. To enhance model fidelity, future work should incorporate higher-resolution wave models and refined turbulence parameterization schemes, and assimilate Argo and satellite remote sensing data to improve the simulation of extreme precipitation, wind stress, and ocean boundary layer processes.

Our findings also illuminate important connections to regional climate variability. The substantial cold wakes and persistent subsurface thermal anomalies induced by typhoons, as quantified in our analysis, can significantly modify air-sea heat fluxes over large areas (Jin et al., 2023). This localized cooling and its subsequent evolution may potentially influence the evolution of regional climate patterns, such as the East Asian monsoon, on sub-seasonal to seasonal timescales. Furthermore, the prolonged ocean response with recovery timescales exceeding 10 d suggests that sequential typhoons may encounter pre-conditioned oceanic environments (Zhang et al., 2013; Kawakami et al., 2022; Wang et al., 2024b). This creates an “ocean memory effect”

that can modulate the intensity of subsequent storms and requires consideration in seasonal climate prediction systems.

Beyond physical processes, our observed vertical mixing and upwelling have significant biogeochemical consequences. The entrainment of nutrient-rich subsurface waters can trigger phytoplankton blooms in the typhoon wake, enhancing primary productivity and carbon export (Wang and Xiu, 2022; Wang et al., 2023b). Conversely, the precipitation-induced freshwater caps may temporarily suppress vertical nutrient supply, creating complex biogeochemical responses that merit further investigation with Argo floats and biogeochemical models. These processes highlight the role of typhoons as intermittent but important drivers of biological productivity and carbon cycling in the oligotrophic ocean.

Additionally, this study is conducted based on only four typhoon cases, which limits the statistical robustness and representativeness of the conclusions. To further verify the observed differences, future research should include a larger collection of samples of typhoons with varying intensities and movement speeds to assess the generality of upper ocean responses in more details. Coupling with climate models could also help evaluate long-term changes in typhoon-ocean interactions under global warming, including potential alterations in typhoon-induced ocean heat redistribution and carbon sequestration (Brizeula et al., 2023; Zhang et al., 2023), providing scientific support for disaster prevention and mitigation efforts.

6 DATA AVAILABILITY STATEMENT

The data used for this study are available from the following sources: CMA best track dataset (https://tcdata.typhoon.org.cn/zjljsjj.html), China Argo profiling float dataset (https://pic.argo.org.cn/), HYCOM GOFS Global Analysis dataset (https://www.hycom.org/dataserver/gofs-3pt1/analysis), HYCOM NCEP CFSR dataset (https://www.hycom.org/dataserver/ncep-cfsr), NASA GPM_3GCSH dataset (https://disc.gsfc.nasa.gov/datasets/GPM_3GCSH_07/summary?keywords=GPM).

7 ACKNOWLEDGMENT

The authors acknowledge the High Performance Computing Center of Nanjing University of Information Science and Technology for their support to this work.

References

Brizeula N G, Alford M H, Xie S P et al. 2023. Prolonged thermocline warming by near-inertial internal waves in the wakes of tropical cyclones. *Proceedings of the National Academy of Sciences of the United States of America*, **120**(26): e2301664120, https://doi.org/10.1073/pnas.2301664120.

Emanuel K A. 1995. Sensitivity of tropical cyclones to surface exchange coefficients and a revised steady-state model incorporating eye dynamics. *Journal of the Atmospheric Sciences*, **52**(22): 3969-3976, https://doi.org/10.1175/1520-0469(1995)052<3969:SOTCTS>2.0.CO;2.

Fan S R, Zhang B, Perrie W et al. 2022. Observed ocean surface winds and mixed layer currents under tropical cyclones: asymmetric characteristics. *Journal of Geophysical Research*: *Oceans*, **127**(2): e2021JC017991, https://doi.org/10.1029/2021JC017991.

Guan S D, Jin F F, Tian J W et al. 2024. Ocean internal tides suppress tropical cyclones in the South China Sea. *Nature Communications*, **15**(1): 3903, https://doi.org/10.1038/s41467-024-48003-y.

Huffman G J, Stocker E F, Bolvin D T et al. 2019. GPM IMERG Final Precipitation L3 Half Hourly 0.1 degree x 0.1 degree V06, Greenbelt, MD, Goddard Earth Sciences Data and Information Services Center (GES DISC), Accessed on 2025-01-01, https://doi.org/10.5067/GPM/IMERG/3B-HH/06.

Intergovernmental Panel on Climate Change. 2021. Climate Change 2021: The Physical Science Basis: Working Group I Contribution to the 6th Assessment Report of the Intergovernmental Panel on Climate Change. Cambridge University Press, Cambridge.

Jin M X, Zhao Z Y, Wu R G et al. 2023. Latitudinal and seasonal variations in tropical cyclone-induced ocean surface cooling in the tropical western North Pacific. *Journal of Meteorological Research*, **37**(6): 790-801, https://doi.org/10.1007/s13351-023-3040-7.

Jyothi L, Joseph S, P S. 2019. Surface and sub-surface ocean response to Tropical Cyclone Phailin: role of pre-existing oceanic features. *Journal of Geophysical Research*: *Oceans*, **124**(9): 6515-6530, https://doi.org/10.1029/2019JC015211.

Kawakami Y, Nakano H, Urakawa L S et al. 2022. Interactions between ocean and successive typhoons in the kuroshio region in 2018 in atmosphere-ocean coupled model simulations. *Journal of Geophysical Research*: *Oceans*, **127**(5): e2021JC018203, https://doi.org/10.1029/2021JC018203.

Kossin J P, Knapp K R, Olander T L et al. 2020. Global increase in major tropical cyclone exceedance probability over the past four decades. *Proceedings of the National Academy of Sciences of the United States of America*, **117**(22): 11975-11980, https://doi.org/10.1073/pnas.1920849117.

Krishnamohan K S, Vialard J, Lengaigne M et al. 2019. Is there an effect of Bay of Bengal salinity on the northern Indian Ocean climatological rainfall? *Deep Sea Research Part II*: *Topical Studies in Oceanography*, **166**: 19-33, https://doi.org/10.1016/j.dsr2.2019.04.003.

Li M Y, He Y J, Liu G Q. 2023. Atmospheric and oceanic responses to Super Typhoon Mangkhut in the South China Sea: a coupled CROCO-WRF simulation. *Journal of Oceanology and Limnology*, **41**(4): 1369-1388, https://doi.org/10.1007/s00343-022-1328-6.

Li X C, Cheng X P, Fei J F et al. 2022. A numerical study on the role of mesoscale cold-core eddies in modulating the upper-ocean responses to typhoon trami (2018). *Journal of Physical Oceanography*, **52**(12): 3101-3122, https://doi.org/10.1175/JPO-D-22-0080.1.

Liu F, Toumi R, Zhang H et al. 2024. Impact of precipitation on ocean responses during a tropical cyclone. *Journal of Physical Oceanography*, **54**(3): 895-909, https://doi.org/10.1175/JPO-D-23-0138.1.

Liu X C, Gu Y Z, Zhai F G et al. 2022. Dramatic temperature variations in the Yellow Sea during the passage of typhoon Lekima (2019). *Estuarine*, *Coastal and Shelf Science*, **269**: 107819, https://doi.org/10.1016/j.ecss.2022.107819.

Lu X Q, Yu H, Ying M et al. 2021. Western North Pacific tropical cyclone database created by the China Meteorological Administration. *Advances in Atmospheric Sciences*, **38**(4): 690-699, https://doi.org/10.1007/s00376-020-0211-7.

Ni Z K, Yu J C, Shang X K et al. 2021. Response of the upper ocean to tropical cyclone in the Northwest Pacific observed by gliders during fall 2018. *Acta Oceanologica Sinica*, **40**(1): 103-112, https://doi.org/10.1007/s13131-020-1672-3.

Pei Y H, Zhang R H, Chen D K. 2015. Upper ocean response to tropical cyclone wind forcing: a case study of typhoon Rammasun (2008). *Science China Earth Sciences*, **58**(9): 1623-1632, https://doi.org/10.1007/s11430-015-5127-1.

Price J F. 1981. Upper ocean response to a hurricane. *Journal of Physical Oceanography*, **11**(2): 153-175, https://doi.org/10.1175/1520-0485(1981)011<0153:UORTAH>2.0.CO;2.

Sun J, Jin S S, Ju X et al. 2024. Influence of spatial heterogeneity in sea surface temperature on tropical cyclone intensity over the western North Pacific. *Journal of Geophysical Research*: *Atmospheres*, **129**(4): e2023JD038971, https://doi.org/10.1029/2023JD038971.

Sun Y T, Cheng D, Yang S Q et al. 2023. Study on ocean response of typhoon hato based on underwater glider observation. *Digital Ocean & Underwater Warfare*, **6**(2): 198-208, https://doi.org/10.19838/j.issn.2096-5753.2023.02.009. (in Chinese with English abstract)

Tan C Y, Zhao H K, Klotzbach P J et al. 2024. Interdecadal shifts in tropical sea surface temperature modulate autumn tropical cyclone genesis over the western North Pacific. *Atmospheric Research*, **306**: 107473, https://doi.org/10.1016/j.atmosres.2024.107473.

Wallcraft A J, Metzger E J, Carroll S N. 2009. Software Design Description for the HYbrid Coordinate Ocean Model (HYCOM), Version 2.2. https://doi.org/10.21236/ada494779.

Wang H P, Li J G, Song J Q et al. 2023a. Ocean response offshore of Taiwan to super typhoon Nepartak (2016) based on multiple satellite and buoy observations. *Frontiers in Marine Science*, **10**: 1132714, https://doi.org/10.3389/fmars.2023.1132714.

Wang H P, Li J G, Song J Q et al. 2024a. Different mechanisms for enhanced ocean response and feedback during sequential super typhoons. *Deep Sea Research Part I*: *Oceanographic Research Papers*, **210**: 104351, https://doi.org/10.1016/j.dsr.2024.104351.

Wang Q Q, Liu J Q, Chen L J et al. 2024b. Upper ocean response to Typhoon Bavi (2008) over western North Pacific. *Journal of Marine Meteorology*, **44**(1): 39-51, https://doi.org/10.19513/j.cnki.hyqxxb.20230605001. (in Chinese with English abstract)

Wang X P, Du Y, Zhang Y H et al. 2023b. Effects of multiple dynamic processes on chlorophyll variation in the Luzon Strait in summer 2019 based on glider observation. *Journal of Oceanology and Limnology*, **41**(2): 469-481, https://doi.org/10.1007/s00343-022-1416-7.

Wang X, Jiang S M, Dai D J et al. 2022. Responses of sea level anomaly to tropical cyclones in Northwest Pacific Ocean. *Advances in Marine Science*, **40**(1): 1-12, https://doi.org/10.12362/j.issn.1671-6647.2022.01.001. (in Chinese with English abstract)

Wang Y T, Xiu P. 2022. Typhoon footprints on ocean surface temperature and chlorophyll-*a* in the South China Sea. *Science of the Total Environment*, **840**: 156686, https://doi.org/10.1016/j.scitotenv.2022.156686.

Wang Z H, Wu K J, Zhao D L. 2024c. Comparative analysis of extreme events of tropical cyclones in the Northwest Pacific Ocean. *Marine Environmental Science*, **43**(5): 755-765, https://doi.org/10.13634/j.cnki.mes.2024.05.001. (in Chinese with English abstract)

Woodruff J D, Irish J L, Camargo S J. 2013. Coastal flooding by tropical cyclones and sea-level rise. *Nature*, **504**(7478): 44-52, https://doi.org/10.1038/nature12855.

Wu Z Y, Gao K, Chen J et al. 2024. Typhoon-induced ocean waves and stokes drift: a case study of typhoon mangkhut (2018). *China Ocean Engineering*, **38**(4): 711-724, https://doi.org/10.1007/s13344-024-0056-4.

Yang B, Hou Y J, Li M. 2019a. Response of the western North Pacific subtropical ocean to the slow-moving super typhoon Nanmadol. *Journal of Oceanology and Limnology*, **37**(3): 938-956, https://doi.org/10.1007/s00343-019-8114-0.

Yang Y J, Fu Y F, Sun L et al. 2010. Responses of the upper ocean to Typhoon Tingting observed from multiplatform satellites and Argo float. *Journal of University of Science and Technology of China*, **40**(1): 1-7, https://doi.org/10.3969/j.issn.0253-2778.2010.01.001. (in Chinese with English abstract)

Yang Y, Li K P, Du J T et al. 2019b. Revealing the subsurface Yellow Sea Cold Water Mass from satellite data associated with Typhoon Muifa. *Journal of Geophysical Research*: *Oceans*, **124**(10): 7135-7152, https://doi.org/10.1029/2018JC014727.

Ye S N, Zhang R H, Wang H N. 2023. The role played by tropical cyclones-induced freshwater flux forcing in the upper-ocean responses: a case for Typhoon Yutu (2018). *Ocean Modelling*, **184**: 102211, https://doi.org/10.1016/j.ocemod.2023.102211.

Ying M, Zhang W, Yu H et al. 2014. An overview of the

China Meteorological Administration tropical cyclone database. *Journal of Atmospheric and Oceanic Technology*, **31**(2): 287-301, https://doi.org/10.1175/JTECH-D-12-00119.1.

Yu J, Zhang H, Chen D K. 2023. Upper ocean response to super typhoon Rammasun (2014) based on Argo data in the South China Sea. *Journal of Marine Sciences*, **41**(2): 14-27, https://doi.org/10.3969/j.issn.1001-909X.2023.02.002. (in Chinese with English abstract)

Zhang H, Chen D K, Zhou L et al. 2016. Upper ocean response to typhoon Kalmaegi (2014). *Journal of Geophysical Research*: *Oceans*, **121**(8): 6520-6535, https://doi.org/10.1002/2016jc012064.

Zhang H, He H L, Zhang W Z et al. 2021. Upper ocean response to tropical cyclones: a review. *Geoscience Letters*, **8**(1): 1, https://doi.org/10.1186/s40562-020-00170-8.

Zhang H, Liu X H, Wu R H et al. 2019a. Ocean response to successive typhoons sarika and haima (2016) based on data acquired via multiple satellites and moored array. *Remote Sensing*, **11**(20): 2360, https://doi.org/10.3390/rs11202360.

Zhang H, Tian D, Sun Y T et al. 2024. Unmanned vehicles probed inner-core air-sea conditions during Super Typhoon Koinu (2023). *Science Bulletin*, **69**(24): 3789-3792, https://doi.org/10.1016/j.scib.2024.10.018.

Zhang H. 2023. Modulation of upper ocean vertical temperature structure and heat content by a fast-moving tropical cyclone. *Journal of Physical Oceanography*, **53**(2): 493-508, https://doi.org/10.1175/JPO-D-22-0132.1.

Zhang L X, Wu X R, Perrie W et al. 2025. Impact of rapid change in the rain-formed barrier layer on the upper ocean thermal response to typhoon kalmaegi (2014). *Journal of Physical Oceanography*, **55**(8): 1193-1209, https://doi.org/10.1175/JPO-D-24-0165.1.

Zhang Q, Liao G H, Lin F L et al. 2019b. Analysis of upper ocean response to Typhoon Doksuri in the northwest South China Sea. *Haiyang Xuebao*, **41**(7): 22-35, https://doi.org/10.3969/j.issn.0253-4193.2019.07.003. (in Chinese with English abstract)

Zhang R H, Pei Y H, Chen D K. 2013. Remote effects of tropical cyclone wind forcing over the western Pacific on the eastern equatorial ocean. *Advances in Atmospheric Sciences*, **30**(6): 1507-1525, https://doi.org/10.1007/s00376-013-2283-0.

Zhang Y H, Liu Y H, Guan S D et al. 2023. Sudden track turning of typhoon Prapiroon (2012) enhanced the upper ocean response. *Remote Sensing*, **15**(2): 302, https://doi.org/10.3390/rs15020302.

Zhou L, Chen D K, Lei X T et al. 2019. Progress and perspective on interactions between ocean and typhoon. *Chinese Science Bulletin*, **64**(1): 60-72, https://doi.org/10.1360/N972018-00668. (in Chinese with English abstract)

Zhu L M, Ke K. 2009. Fluid Mechanics. Shanghai: Tongji University Pub. (in Chinese)